A Microstructure-Based Constitutive Model for Superplastic Forming

REZA JAFARI NEDOUSHAN, MAHMOUD FARZIN, MOHAMMAD MASHAYEKHI, and DOREL BANABIC

A constitutive model is proposed for simulations of hot metal forming processes. This model is constructed based on dominant mechanisms that take part in hot forming and includes intergranular deformation, grain boundary sliding, and grain boundary diffusion. A Taylor type polycrystalline model is used to predict intergranular deformation. Previous works on grain boundary sliding and grain boundary diffusion are extended to drive three-dimensional macro stress–strain rate relationships for each mechanism. In these relationships, the effect of grain size is also taken into account. The proposed model is first used to simulate step strain-rate tests and the results are compared with experimental data. It is shown that the model can be used to predict flow stresses for various grain sizes and strain rates. The yield locus is then predicted for multiaxial stress states, and it is observed that it is very close to the von Mises yield criterion. It is also shown that the proposed model can be directly used to simulate hot forming processes. Bulge forming process and gas pressure tray forming are simulated, and the results are compared with experimental data.

I. INTRODUCTION

HOT forming processes, including superplastic forming (SPF) and quick-plastic forming (QPF), are used to manufacture components with complex shapes that usually cannot be produced by cold forming. Especially superplastically formed parts find many applications, particularly in aerospace and transportation industries, where weight reduction is critical to meet product performance requirements.[1,2] Finite-element simulations of hot forming are of great interest as a tool for process design. In hot forming, many parameters affect the flow stress such as strain rate, temperature, and microstructure. Therefore, the accuracy of constitutive models is currently the most significant issue in forming simulations. There is also great interest in developing a better understanding of the dominant mechanisms responsible for hot forming to extend desirable forming conditions.

Constitutive models of hot forming have been historically constructed from uniaxial tension tests.[1–5] In these works, several tests are performed on materials with various microstructures, temperatures, and strain rates. Then, a function is fitted to the resulting data. This function in conjunction with a potential surface that relates different stress states to an equivalent stress is used to predict material behavior in various situations.[6–13]

Researchers have tried to improve their understanding about dominant mechanisms responsible for hot forming by developing microstructural constitutive models. In practice, it has been noticed that microstructural forming mechanisms affect the stress–strain rate relation. Chandra[14] proposed a constitutive model that considered microstructural forming mechanisms and compared it with other available constitutive models. Some researchers developed a microstructural-based model and investigated superplastic forming mechanisms.[15–19] More investigations showed that mechanisms of deformation in hot forming and especially superplastic forming differ substantially from cold forming.[14] Besides deformation within the grains, which is the dominant mechanism in cold forming, other mechanisms may play a role in hot forming, including grain boundary sliding, grain boundary diffusion, and grain boundary migration.

Many researchers considered the contribution of intergranular deformation as well as grain boundary sliding in total deformation and obtained a better fit to tensile test data.[20–23] Some others also considered contribution of grain boundary diffusion.[14,16]

The aim of the current work is to propose a constitutive model based on microstructural mechanisms that can predict material behavior for various grain sizes and strain rates. Although this model considers micromechanisms, it can be directly used in hot forming simulations and does not need multiscale modeling as discussed in Reference 19. In the current work, experimental data on an aluminum–magnesium alloy, i.e., AA5083 at 723 K (450 °C) are used to

REZA JAFARI NEDOUSHAN, PhD Student, MAHMOUD FARZIN, Professor, and MOHAMMAD MASHAYEKHI, Assistant Professor, are with the Department of Mechanical Engineering, Isfahan University of Technology, Isfahan, 84156 Iran. DOREL BANABIC, Professor, is with the Mechanical Technology Department, Technical University of Cluj-Napoca, 3400 Cluj-Napoca, Romania. Contact e-mail: banabic@tcm.utcluj.ro
Manuscript submitted July 30, 2011.

calibrate and validate the model. Strain hardening, which is typically associated with grain growth during hot forming, was observed to be small over the temperature, strains, and strain rates under consideration for this material.[24] Therefore, it can be concluded that the effect of boundary migration is small in this case. This material has also proved to be free of any dynamic recrystallization effects for the conditions considered in the current investigation.[24–26] Therefore, to prepare the constitutive model in this article, from the previously mentioned mechanisms, the following three are considered to be more important: intergranular deformation, grain boundary sliding (GBS), and grain boundary diffusion (GBD).

In the current work, intergranular deformation is predicted by the Taylor type polycrystalline approach. This approach is widely used to predict polycrystalline material behavior in cold-forming processes without considering the effect of grain boundaries.[27–32]

For the GBS mechanism, a new approach is proposed to correlate macro strain rates to macro stresses. In this approach, boundaries are considered as parallel planes, and it is assumed that slide occurs on these planes. A grain size effect on stress–strain rate relationship is also considered.

For the GBD mechanism also, a new three-dimensional (3-D) relationship between macro strain rate and macro stress is derived by extending works by Cocks,[33] Pan and Cocks,[34] and Bower and Wininger.[16] A grain size effect has also been taken into account in this relationship. It is shown that for this mechanism, the proposed stress–strain rate relationship obeys the Prandtl-Reuss flow rule.

The available constitutive models that include material dependency of strain rate and grain size are applicable for limited conditions of forming. For example, some of these relations can explain material constitutive behavior when the logarithmic scale of stress and strain rate diagram is a straight line. Some other relations can only be used for certain grain sizes.[35] In contrast, there are also some microstructure-based models that cannot be used in the simulation of real 3-D processes. The proposed strain rate and grain size dependant constitutive model can be used for a vast range of forming conditions. The model is calibrated with a few experiments for the whole range of its application. It has been used to simulate real processes. Another advantage of the proposed model is that it does not presume any yield locus and automatically predicts the yield locus.

The remainder of this article is organized as follows: First, assumptions and the governing equations are listed for the three previously mentioned mechanisms separately. Then, step strain-rate tests are simulated to show the capability of the model in various strain rates and grain sizes. The yield locus is then predicted for multiaxial stress states, and it is shown that it is very close to the von Mises yield criterion. Also, to validate the model in multiaxial stress state conditions, a bulge test and gas pressure tray forming are simulated. The results of the previously mentioned simulations are compared with experimental observations.

II. MODEL DESCRIPTION

In the proposed model, a material point is visualized as a representative of grains and their boundaries. So the macroscopic deformation is a result of intergranular deformation caused by dislocations creep, GBS, and GBD, at that point. In the current work it is assumed that the three mentioned mechanisms operate separately; therefore, the resulted velocity field of each mechanism can be calculated separately. Furthermore, the total velocity field is sum of the entire mentioned velocity fields. Therefore, the velocity gradient is also the sum of the velocity gradients of each mechanism.

$$L_{ij} = L_{ij}^{CR} + L_{ij}^{GBS} + L_{ij}^{GBD} \qquad [1]$$

where L_{ij} denotes the total velocity gradient tensor, L_{ij}^{CR} is the velocity gradient due to intergranular deformation, L_{ij}^{GBS} is the velocity gradient caused by GBS, and L_{ij}^{GBD} is the GBD velocity gradient.

A. Intergranular Deformation

The Taylor type polycrystalline approach with a standard crystal plasticity model is used to approximate the response of material within the grains.

1. Single-crystal constitutive model

The crystal plasticity model used in this work employs the framework of classical crystal plasticity by Peirce et al.,[36,37] Asaro,[38] and Asaro et al.[39] Implementation of this model is based on the user-material routine (UMAT) of Huang[40] in the environment of finite-element code ABAQUS. In this article, the grains are all face-centered cubic (fcc) crystals, with 12 (1 1 1) [1 1 0] slip systems.

The total deformation of a crystallite is a result of two distinct physical mechanisms: crystallographic plastic slips caused by dislocation motions on the active slip systems and elastic lattice distortion. Each grain deforms plastically by shearing on a set of N slip systems, which are characterized by unit vectors normal to the slip plane m_i^α and unit vectors parallel to the slip direction s_i^α, in the initial configuration. The superscript α indicates a slip system and ranges from 1 to N. In the plastic deformation, it is assumed that slips system's vectors m_i^α and s_i^α remain not only undistorted but also unrotated. Next, the material and lattice are considered to deform elastically and rotate rigidly from the plastically deformed state to the current configuration. Hence, the deformation gradient F_{ij} is written as follows:

$$F_{ij} = F_{ik}^e F_{kj}^p \qquad [2]$$

where F_{ik}^e and F_{kj}^p represent elastic and plastic deformation, respectively. The velocity gradient, therefore, decomposes into elastic and plastic parts as

$$L_{ij}^{CR} = \dot{F}_{ik} F_{kj}^{-1} = \dot{F}_{ik}^e F_{kj}^{e-1} + F_{ik}^e \dot{F}_{kl}^p \dot{F}_{lm}^{p-1} F_{mj}^{e-1} = L_{ij}^e + L_{ij}^p$$

$$[3]$$

$$L_{ij}^e = \dot{F}_{ik}^e F_{kj}^{e-1} \qquad [4]$$

$$L_{ij}^{\mathrm{p}} = F_{ik}^{\mathrm{e}}\dot{F}_{kl}^{\mathrm{p}}\dot{F}_{lm}^{\mathrm{p}-1}F_{mj}^{\mathrm{e}-1} \qquad [5]$$

The symmetric and antisymmetric parts of velocity gradient tensor can also be decomposed into elastic and plastic parts.

$$D_{ij}^{\mathrm{CR}} = D_{ij}^{\mathrm{e}} + D_{ij}^{\mathrm{p}} \qquad [6a]$$

$$W_{ij}^{\mathrm{CR}} = W_{ij}^{\mathrm{e}} + W_{ij}^{\mathrm{p}} \qquad [6b]$$

It is convenient to define the vectors $\left(s_i^{*\alpha}, m_i^{*\alpha}\right)$, denoting the slip system α in the deformed configuration.

$$s_i^{*\alpha} = F_{ij}^{\mathrm{e}}s_j^{\alpha} \qquad [7a]$$

$$m_j^{*\alpha} = m_i^{\alpha}F_{ij}^{\mathrm{e}-1} \qquad [7b]$$

By introducing the following symmetric and antisymmetric tensors for each slip system α.

$$P_{ij}^{\alpha} = \frac{1}{2}\left(s_i^{*\alpha}m_j^{*\alpha} + s_j^{*\alpha}m_i^{*\alpha}\right) \qquad [8a]$$

$$w_{ij}^{\alpha} = \frac{1}{2}\left(s_i^{*\alpha}m_j^{*\alpha} - s_j^{*\alpha}m_i^{*\alpha}\right) \qquad [8b]$$

The plastic deformation rate and spin for the crystal can be written, respectively, as

$$D_{ij}^{\mathrm{P}} = \sum_{\alpha=1}^{N}\dot{\gamma}^{\alpha}P_{ij}^{\alpha} \qquad [9a]$$

$$W_{ij}^{\mathrm{P}} = \sum_{\alpha=1}^{N}\dot{\gamma}^{\alpha}w_{ij}^{\alpha} \qquad [9b]$$

where $\dot{\gamma}^{\alpha}$ is the slip rate of a generic system and is computed from the following:

$$\dot{\gamma}^{\alpha} = \dot{\gamma}_0^{\alpha}\left(\frac{\tau^{\alpha}}{\tau_0}\right)^{k_1} \qquad [10]$$

where $\dot{\gamma}_0^{\alpha}$ is a characteristic slip rate, k_1 is the stress exponent of the slip system and τ_0 is a characteristic flow strength. Hardening is neglected in the current computations and τ_0 is assumed to be constant. τ^{α} is resolved shear stress on the slip system α and is computed from the following:

$$\tau^{\alpha} = P_{ij}^{\alpha}\sigma_{ij} \qquad [11]$$

where σ_{ij} is the Cauchy stress. The elastic constitutive equation for a crystal is specified by

$$\hat{T}_{ij} = \dot{T}_{ij} - W_{im}^{\mathrm{e}}T_{mj} + T_{im}W_{mj}^{\mathrm{e}} = C_{ijkl}D_{kl}^{\mathrm{e}} \qquad [12]$$

where $\hat{T}_{ij}$ is the Jaumann rate of the Kirchhoff stress tensor considering the lattice rotations and C_{ijkl} is the tensor of the elastic moduli. For the case of fcc grains,

the elastic properties are specified by values of Young's modulus E, Poisson's ratio v, and shear modulus μ with respect to a coordinate system aligned with the [1 0 0] directions.

2. Polycrystalline model

For polycrystalline materials, a material point can be visualized as a multitude of single crystals, and the constitutive response at this material point is taken as a suitable average of the constitutive response of the individual crystals comprising this representative point. Various averaging procedures have been proposed in the literature to make this transition from the microresponse of the individual grains to the macroresponse of the polycrystalline aggregate.[41–44] In the current work, among these models, the Taylor type model[44] is used to calculate the crystal or intergranular deformation. In this model, the deformation in each grain is taken to be identical to the macroscopic granular contribution of deformation.

$$D_{ij}^{\mathrm{CR}} = D_{ij}^{\mathrm{ma}} - D_{ij}^{\mathrm{GBS}} - D_{ij}^{\mathrm{GBD}} \qquad [13a]$$

$$W_{ij}^{\mathrm{CR}} = W_{ij}^{\mathrm{ma}} - W_{ij}^{\mathrm{GBS}} - W_{ij}^{\mathrm{GBD}} \qquad [13b]$$

In other words, according to Eqs. [13a] and [13b], D_{ij}^{CR} is calculated using the macroscopic deformation rate D_{ij}^{ma} and after subtracting the deformation rates resulting from boundary mechanisms,. A spin tensor in each grain is also calculated in a similar way.

Furthermore, the macroscopic values of all quantities, such as stresses, stress rates, and elastic modules, are obtained by averaging their respective values over grains with random orientations at that particular material point.

$$\sigma_{ij}^{\mathrm{ma}} = \frac{\sum_1^{N_g}\sigma_{ij}^{\mathrm{CR}}}{N_g} \qquad [14]$$

where N_g is the total number of random directions considered at that material point. In the current work, $N_g = 70$; in other words, 70 random directions were considered at a given material point.

B. Grain Boundary Sliding

Grain boundary sliding occurs because the shear tractions act tangent to the grain boundary. For calculating GBS deformation in a material point, the following is assumed:

(a) The boundaries are composed of parallel planes in several presumed directions at a material point. So, a set of normal vectors indicates the boundaries. Figure 1 illustrates this simplification in two dimensions. In the current work, it is assumed that in each of xy, zy, and xz planes the grain is an eight-sided polygon that consequently has four parallel boundaries. Figure 2 shows these boundaries in the xy plane and Table I shows all boundary normal vectors.
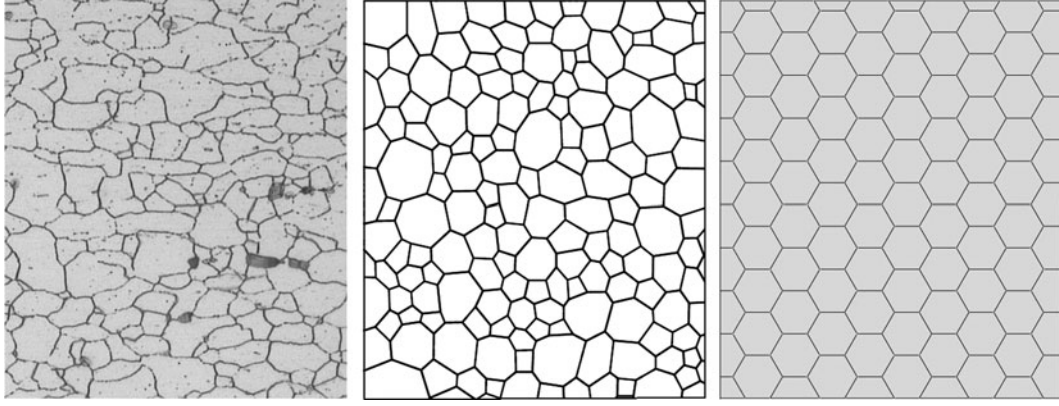
Fig. 1—Visualizing grain boundaries as parallel planes, illustrated in two dimensions.
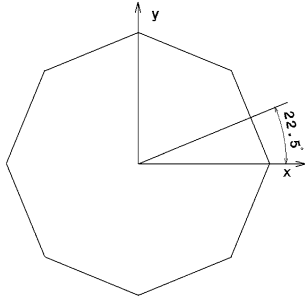

Fig. 2—Assumed grain boundaries in xy plane as an example.

Table I. Assumed Boundary Normal Vectors

Boundary Number β	n_1^β	n_2^β	n_3^β
1	a*	b†	0
2	b	a	0
3	–a	b	0
4	–b	a	0
5	0	a	b
6	0	b	a
7	0	–a	b
8	0	–b	a
9	a	0	b
10	b	0	a
11	a	0	–b
12	b	0	–a

*a = cos(22.5).
†b = sin(22.5).

(b) Stress tensor is identical for all boundaries and is equal to the macro stress in the material point.
(c) Relative sliding velocity between two grains has the same direction with shear traction acting on the boundary.

Shear traction acting on all parallel boundaries with a normal vector n_i^β can be calculated as follows:

$$\tau_i^\beta = \sigma_{ij} n_j^\beta - \left(\sigma_{mj} n_m^\beta n_j^\beta\right) n_i^\beta = \sigma_t^\beta t_i^\beta \qquad [15]$$

The superscript β indicates the number of assumed boundary planes which ranges from one to 12 in this case. Here, σ_t^β is the resolved shear stress and t_i^β is direction of this shear traction.

If the resolved shear stress in these boundaries is greater than a threshold stress σ_{th}, then the following viscous constitutive equation is assumed to characterize sliding. This equation relates the relative sliding velocity of two adjacent grains to the resolved shear stress by

$$\begin{cases} v_t^\beta = \frac{\Omega \eta \exp(-Q_{GBS}/kT)}{kT} \left(\frac{\sigma_t^\beta - \sigma_{th}}{\sigma_{th}}\right)^{n_1} & \text{if} \quad \sigma_t^\beta > \sigma_{th} \\ v_t^\beta = 0 & \text{if} \quad \sigma_t^\beta < \sigma_{th} \end{cases} \qquad [16]$$

where η is a characteristic sliding velocity, k is the Boltzmann constant, T is the absolute temperature, n_1 is the stress exponent of the slid, Ω is the atomic volume, and Q_{GBS} is the activation energy for GBS. The shear strain rate from GBS in all parallel boundary planes with a normal vector n_i^β can be written as follows:

$$\dot{\gamma}^\beta = \frac{v_t^\beta}{d} \qquad [17]$$

where d is the average grain size. The macro deformation rate from GBS in these parallel boundaries can be written as follows:

$$D_{ij}^\beta = \frac{1}{2}\dot{\gamma}^\beta \left(n_i^\beta t_j^\beta + t_i^\beta n_j^\beta\right) \qquad [18a]$$

$$W_{ij}^\beta = \frac{1}{2}\dot{\gamma}^\beta \left(n_i^\beta t_j^\beta - t_i^\beta n_j^\beta\right) \qquad [18b]$$

Considering all boundaries:

$$D_{ij}^{GBS} = \frac{1}{2}\sum_{\beta=1}^{N_b} \dot{\gamma}^\beta \left(n_i^\beta t_j^\beta + t_i^\beta n_j^\beta\right) \qquad [19a]$$

$$W_{ij}^{GBS} = \frac{1}{2}\sum_{\beta=1}^{N_b} \dot{\gamma}^\beta \left(n_i^\beta t_j^\beta - t_i^\beta n_j^\beta\right) \qquad [19b]$$

where N_b is 12 in this case. It should be emphasized that GBS deformation is entirely plastic, and there is no elastic deformation caused by GBS. It is also worth mentioning that assuming a higher number of slide directions than 12 had no significant change in the results. Therefore, only 12 slide directions were enough in the current modeling.

C. Grain Boundary Diffusion

Figure 3 shows a grain boundary between two adjacent grains. The atoms (or equivalently, vacancies) adjacent to the grain boundary are assumed to be mobile. Atoms may detach from each grain, diffuse along the boundary, and then reattach to one of the two adjacent grains.[16] In this process, the atoms detach from regions of the grain boundary that are subjected to compressive stress and migrate to regions that are under tensile stress.[18,33,34] Hence, grain boundary diffusion is assumed to be a function of variation of the normal stress acting on the boundary.

Therefore, it is assumed that the flux of atoms tangent to each interface is related to the normal stress[16,18] through

$$j = -\frac{\Omega D_{\mathrm{GB}t}\delta_{\mathrm{GB}}\exp(-Q_{\mathrm{GB}t}/\mathrm{k}T)}{2\mathrm{k}T}\frac{\partial \sigma_n}{\partial s} \qquad [20]$$

where T is absolute temperature, k is Boltzmann constant, $D_{\mathrm{GB}t}\exp(-Q_{\mathrm{GB}t}/\mathrm{k}T)$ is the tangential grain boundary diffusivity, $Q_{\mathrm{GB}t}$ is the corresponding activation energy, and $\delta_{\mathrm{GB}}/2$ is the thickness of the diffusion layer in one grain. When the temperature is constant, Eq. [20] can be simplified

$$j = -\mathrm{q}\frac{\partial \sigma_n}{\partial s} \qquad [21]$$

where q is a constant. Considering mass conservation, the velocity discontinuity in the direction of the normal to the grain boundary is

$$[v_n] = -\frac{\partial j}{\partial s} = \mathrm{q}\frac{\partial^2 \sigma_n}{\partial s^2} \qquad [22]$$

Remembering that a material point was visualized as an aggregate of grains with their boundaries for calculating GBD deformation, the following is assumed:
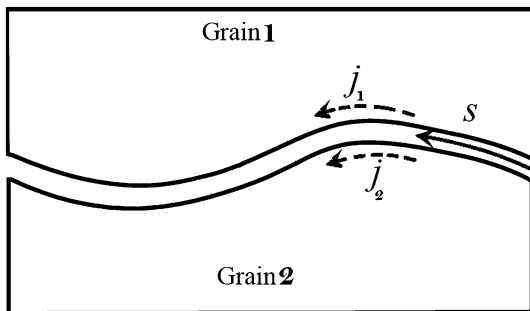

Fig. 3—A two-dimensional grain boundary and flux of atom along the boundary.

(a) Deformation caused by GBD in a material point can be replaced by deformation that occurs in one grain by GBD. With this assumption, the atoms only move around one grain and cannot move from one grain to another one; in addition, grain boundary migration is not modeled. With this assumption, grain boundaries cannot exchange atoms at triple junctions and satisfaction of mass conservation at triple junctions does not need to be considered.
(b) The grain has a spherical shape.
(c) Stress is constant around the grain boundary and equals the macro stress at that material point.

With these assumptions, a grain boundary is a two-dimensional space (spherical surface), and Eqs. [21] and [22] are extended for a two-dimensional space.

$$\vec{j} = -\mathrm{q}\vec{\nabla}\sigma_n = -\mathrm{q}\left(\frac{\partial \sigma_n}{\partial s_1}e_1 + \frac{\partial \sigma_n}{\partial s_2}e_2\right) \qquad [23]$$

$$[v_n] = -\mathrm{q}\left(\frac{\partial^2 \sigma_n}{\partial s_1^2} + \frac{\partial^2 \sigma_n}{\partial s_2^2}\right) \qquad [24]$$

where e_1 and e_2 are unit base vectors on the boundary that is a two-dimensional space, and s_1 and s_2 are lengths along e_1 and e_2. Normal stress is

$$\sigma_n = \sigma_{ij}n_i n_j \qquad [25]$$

where **n** is normal vector of the sphere surface. Considering that stress is constant around the boundary, from Eq. [24], the velocity discontinuity can be written as follows:

$$[v_n] = -2\mathrm{q}\sigma_{ij}\left(\frac{\partial n_i}{\partial s_1}\cdot\frac{\partial n_j}{\partial s_1} + n_i\cdot\frac{\partial^2 n_j}{\partial s_1^2} + \frac{\partial n_i}{\partial s_2}\cdot\frac{\partial n_j}{\partial s_2} + n_i\cdot\frac{\partial^2 n_j}{\partial s_2^2}\right)$$
$$= -2q\sigma_{ij}\alpha_{ij} \qquad [26]$$

$$\alpha_{ij} = \frac{\partial n_i}{\partial s_1}\cdot\frac{\partial n_j}{\partial s_1} + n_i\cdot\frac{\partial^2 n_j}{\partial s_1^2} + \frac{\partial n_i}{\partial s_2}\cdot\frac{\partial n_j}{\partial s_2} + n_i\cdot\frac{\partial^2 n_j}{\partial s_2^2} \qquad [27]$$

where σ_{ij} is a symmetric tensor; therefore

$$[v_n] = -2\mathrm{q}\sigma_{ij}\lambda_{ij} \qquad [28]$$

$$\lambda_{ij} = \frac{1}{2}\left(\alpha_{ij} + \alpha_{ji}\right) \qquad [29]$$

To calculate deformation from GBD at a material point, consider a surface element da with a normal vector **n**. In this work, it is assumed that velocity discontinuity causes elongation (or compression) of an element of sphere with a surface da and length d as shown in Figure 4. The deformation rate tensor of this element in local Cartesian coordinate constructed in the direction of **n** can be written as follows:

$$D_{11}'^{da} = \frac{[v_n]}{d} \qquad D_{ij}'^{da} = 0 \quad i \neq 1, j \neq 1 \qquad [30]$$
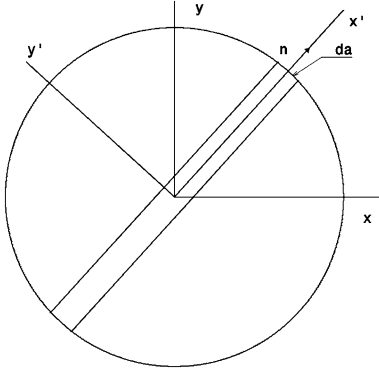
Fig. 4—Deformation caused by GBD on a surface element on the spherical grain.

Evidently, the spin tensor is zero and also the diffusion process is entirely plastic. Considering Eq. [30], the deformation rate tensor can be transformed to a global coordinate as follows:

$$D_{ij}^{da} = a_{im}a_{jn}D_{mn}^{'da} = a_{i1}a_{j1}D_{11}^{'da} = D_{11}^{'da}n_i n_j \qquad [31]$$

$$a_{im} = e_i \cdot e_m' \qquad [32]$$

where e_m' are base vectors in local coordinate and e_i are base vectors in global coordinates. The total GBD deformation rate in a spherical grain is, therefore

$$D_{ij}^{GBD} = \frac{1}{A_s}\iint_{A_s} D_{ij}^{da}da = \frac{1}{A_s}\iint_{A_s} \frac{[v_n]}{d} n_i n_j da$$
$$= \frac{-2q\sigma_{mn}}{A_s d}\iint_{A_s} \lambda_{mn}n_i n_j da = R_{ijmn}\sigma_{mn} \qquad [33]$$

where A_s is the sphere surface. The fourth order tensor R_{ijmn} can be calculated by integrating over the grain surface

$$R_{ijmn} = \frac{-2q}{A_s d}\iint_{A_s} \lambda_{mn}n_i n_j da \iint = \frac{K}{d^3}\iint_{A_s} \lambda_{mn}n_i n_j da \quad [34]$$

In Voigt notation:

$$D_{ij} = D_{ij}^{CR} + D_{ij}^{GBS} + D_{ij}^{GBD} \qquad [36a]$$

$$W_{ij} = W_{ij}^{CR} + W_{ij}^{GBS} \qquad [36b]$$

Equations [36a] and [36b] show the effect of strain rate on the flow stress considering three dominant deformation mechanisms independently. They also predict effect of grain size on the flow stress for GBD and GBS mechanisms. Equations [17] and [35] show the effect of grain size on the flow stress for GBS and GBD mechanisms, respectively. According to these equations, the effect of grain size for GBD mechanism is much stronger than GBS, which is in agreement with the experimental results as will be discussed subsequently.

III. NUMERICAL IMPLEMENTATION

To add the proposed constitutive equations to the Abaqus finite element method (FEM) code, a user subroutine UMAT is used. For intergranular deformation, Huang UMAT[40] is used. To include GBD and GBS, the following algorithm shown in Figure 5 is used. In this algorithm $d\varepsilon_{ij}^t$ is total strain increment, $d\varepsilon_{ij}^{GBD}$ is strain increment from GBD, $d\varepsilon_{ij}^{GBS}$ is the GBS strain increment, and $d\varepsilon_{ij}^{Cr}$ is the strain increment caused by intergranular deformation. $\frac{\partial \Delta\sigma}{\partial \Delta\varepsilon^{Cr}}$, is the Jacobean and is calculated from the Taylor model. It can be easily shown that is equal to which is the total Jacobean. θ is a character that shows GBS and GBD are calculated from the stress at the beginning or the end of the increment. For example, if $\theta = 0$, GBS and GBD are calculated from the stress value at the beginning of the increment and if $\theta = 1$, the stress value at the end of the increment will be used. In this work, $\theta = 0.5$ has been used.

IV. APPLICATIONS AND RESULTS

In this section, the proposed model is used in various stress states, and the capability and/or limitations of the

$$
\begin{bmatrix} D_{11}^{GBD} \\ D_{22}^{GBD} \\ D_{33}^{GBD} \\ 2D_{12}^{GBD} \\ 2D_{13}^{GBD} \\ 2D_{23}^{GBD} \end{bmatrix} = \frac{1.6755K}{d^3}\begin{bmatrix} 2 & -1 & -1 & 0 & 0 & 0 \\ -1 & 2 & -1 & 0 & 0 & 0 \\ -1 & -1 & 2 & 0 & 0 & 0 \\ 0 & 0 & 0 & 6 & 0 & 0 \\ 0 & 0 & 0 & 0 & 6 & 0 \\ 0 & 0 & 0 & 0 & 0 & 6 \end{bmatrix}\begin{bmatrix} \sigma_{11} \\ \sigma_{22} \\ \sigma_{33} \\ \sigma_{12} \\ \sigma_{13} \\ \sigma_{23} \end{bmatrix} = \frac{1.6755K}{3d^3}\begin{bmatrix} S_{11} \\ S_{22} \\ S_{33} \\ 2S_{12} \\ 2S_{13} \\ 2S_{23} \end{bmatrix} \qquad [35]
$$

where S_{ij} is the deviatory stress tensor. This relation is exactly similar to the Prandtl-Reuss flow rule and satisfies incompressibility and isotropy conditions. Equation [1] can be rewritten as follows:

model are investigated. Step strain-rate tensile tests are simulated first for calibration and subsequent validation of the model and then the hydrostatic bulge test is simulated as a multiaxial stress state test.
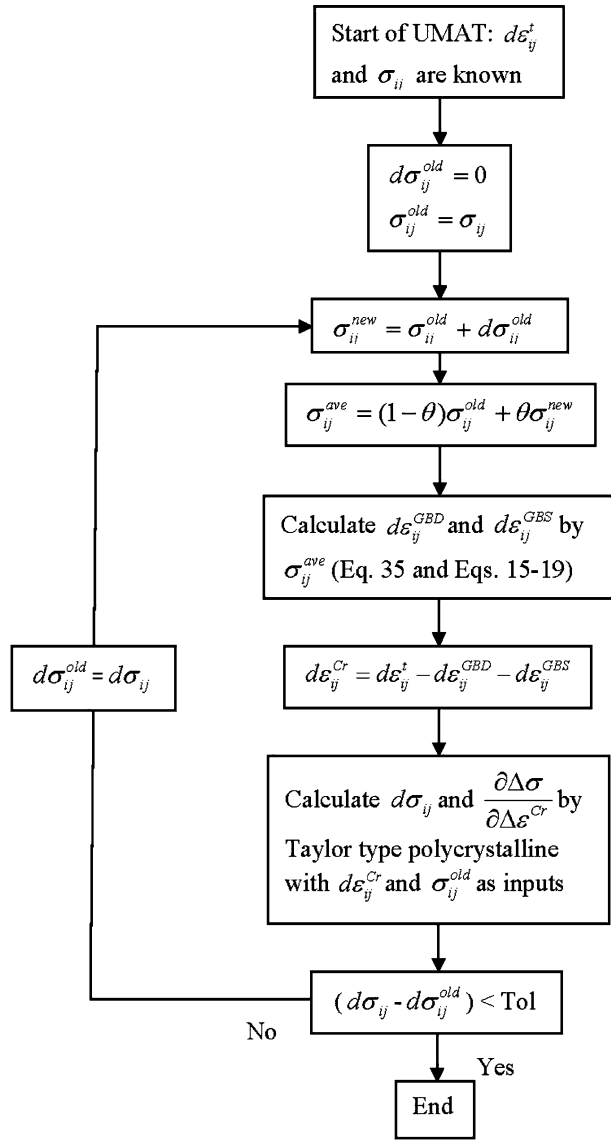
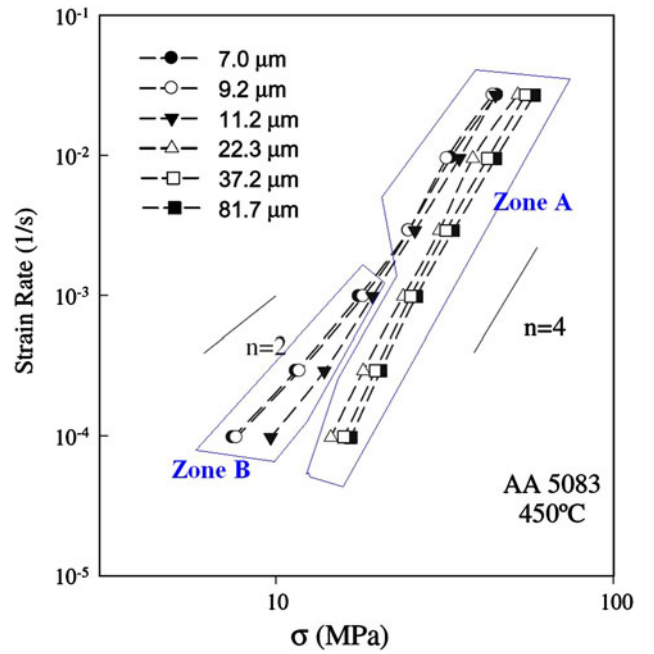Fig. 5—Numerical algorithm used to implement constitutive equations in Abaqus software.

Fig. 6—Step strain-rate tests results for AA5083, from Krajewski et al.[19]

where A is a material constant and n is the stress exponent. The material constants A and n are functions of strain rate, grain size, and temperature. The data in Figure 6 suggest that material behavior can be classified into two distinct zones:

(a) For grain sizes greater than 22.3 μm and also at fast strain rates, data can be fitted with a stress exponent n = 4. For these conditions, material behavior is less sensitive to grain size, as is shown by zone A in Figure 6.

(b) At slow strain rates and grain sizes finer than 22.3 μm, material behavior is more sensitive to grain size and has a lower stress exponent. In the current work, this zone is called zone B.

The change in stress exponent in these two zones suggests a transition in the deformation mechanism. More evidence has been obtained for such a mechanism transition from the deformation and failure characteristics of the specimens.[15,26]

The step strain-rate tensile test is simulated by ABAQUS FEM code with a cubic specimen of length a. The material behavior is implemented in this code through a UMAT. The material is subjected to boundary loading, which approximates uniaxial tension. As can be observed in Figure 7, symmetry conditions are applied on planes $x = 0$, $y = 0$, and $z = 0$. There is no traction on planes $y = a$ and $z = a$, and the cube is subjected to a constant strain rate by displacing the plane at $x = a$. The following velocity is applied to the plane at $x = a$ to obtain a constant strain rate $\dot{\varepsilon}$

$$v = a\dot{\varepsilon}\exp(\dot{\varepsilon}t) \qquad [38]$$

where t is time. The velocity in Eq. [38] is implemented in the ABAQUS FEM code through a UAMP.
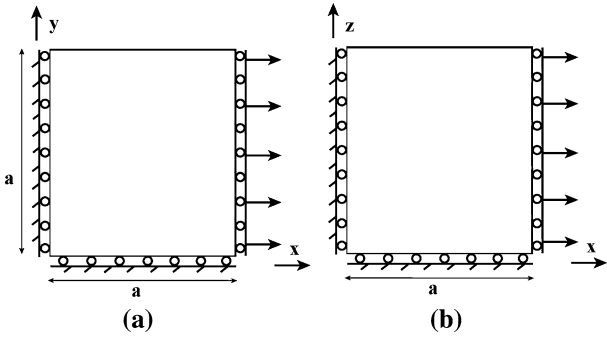
A. Simulation of Step Strain-Rate Tensile Tests

In step strain-rate tensile tests, a series of strain rates is imposed on a single specimen to obtain flow stress as a function of the temperature, strain, and strain rate. In the step strain-rate tests used in current work, after changing the strain rate, the strain rate remains constant until the material pass its transition zone and stress become stable. Additional details of the step strain-rate testing procedure are described in References 15 and 19. The flow stress *vs* strain rate data of AA5083 derived from the step strain-rate testing procedure by Krajewski et al.[19] are shown in Figure 6. These experimental data will be used for comparison with the predicted results in this article. Considering Figure 6, the data at constant temperature can fit approximately a creep law of the form

$$\dot{\varepsilon} = A\sigma^{n} \qquad [37]$$

METALLURGICAL AND MATERIALS TRANSACTIONS A

Fig. 7—Boundary conditions, used in FE simulation (*a*) in *xy* plane (*b*) in *xz* plane.

Table II. Calibrated Parameters Used in the Current Simulations

Parameter	Value
Temperature T	723 K (450 °C)
Young's modulus E	70000 Mpa
Poisson's ratio v	0.3
Characteristic strain rate $\dot{\gamma}_0$	$6 s^{-1}$
Slip system strength τ_0	65 Mpa
Stress exponent of slip k_1	4.35
Stress exponent of boundary slide n_1	3.6
Grain boundary sliding pre-exponential η	$1.8683\ Jsm^{-2}$
Grain boundary sliding activation energy Q_{GBS}	1.34 e-19 J
Atomic volume Ω	1.66 e-29 m^3
Grain boundary diffusion coefficient K	$1.34\ e\text{-}2\ Nm^{-3}\ s^{-1}$
Threshold stress of boundary slide σ_{th}	0.2 MPa

The constitutive parameters used in these simulations were calibrated with the following data:

- Data of grain size 81.7 μm for various strain rates (6 points)
- Data of grain size 7 μm with strain rates of 0.0001 and 0.03 1/s (2 points)

It has been shown experimentally by Agarwal *et al.*[15] that for high strain rates and larger grain sizes, grain boundary mechanisms have no significant effects. Therefore, to guess parameter values initially, the points with grain size of 81.7 μm and strain rates more than 0.001 1/s are used to find intergranular parameters including: $\dot{\gamma}_0$, τ_0, and k_1. Then, using the obtained parameters, several trials were performed to find grain boundary parameters including n_1, η, K, and to obtain the best fit to the rest of the selected data.

After the steps mentioned, the final parameter values are estimated through several trials by using the previously guessed parameters. For this purpose, a script was written in Python. In this script for each set of parameters, stress is calculated for each selected point. Then, the best set of parameters is selected by the least-square method and comparing the stress values with the
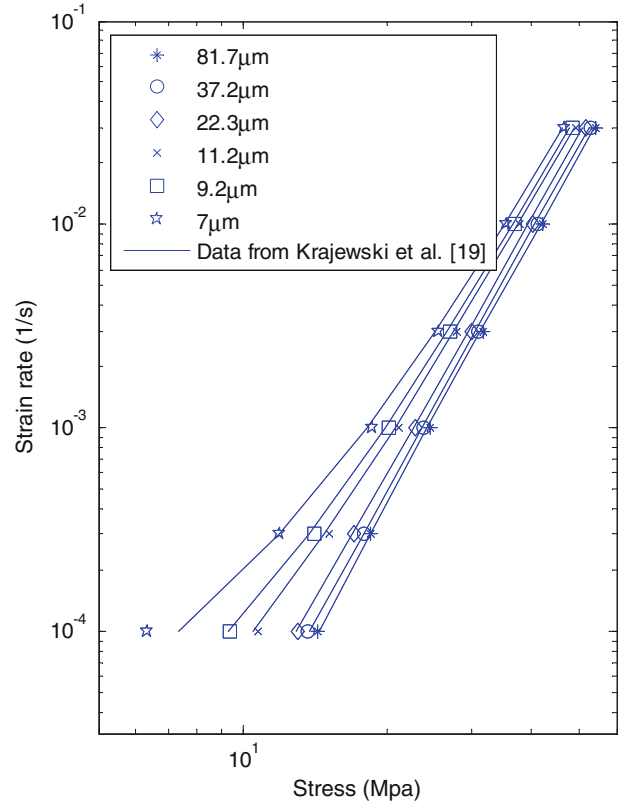

Fig. 8—Comparison of current simulations results with Krajewski *et al.*'s data.[19]

experimental stresses. Table II shows the final parameters obtained by this method.

The same material properties were then used to predict the behavior of specimens with other grain sizes. The predictions of current simulations are compared with Krajewski *et al.*'s[19] results as shown in Figure 8. They are in close agreement for both two distinct zones, A and B.

To investigate the effect of GBD, simulations are performed with and without this mechanism. Simulation results without GBD are compared with Krajewski *et al.*'s data in Figure 9. In these simulations, the parameters in Table II are also used. Simulations without GBD predict flow stresses near the experimental results for grain sizes greater than 22.3 μm. Therefore, the effect of GBD can be ignored for these grain sizes. The simulation results without GBD also match the experiments for grain sizes smaller than 22.3 μm but with strain rates of more than 0.001 1/s. However, for lower strain rates, simulations predict a higher flow stress than experiments.

Therefore, GBD is effective only for materials with grain sizes of 11.2 μm or finer grains and also strain rates less than 0.001 1/s. These circumstances are exactly the limits that characterize zone B, observed in experiments. In zone A, GBD mechanism approximately has no effect, and intergranular deformation and GBS are dominant mechanisms of deformation.
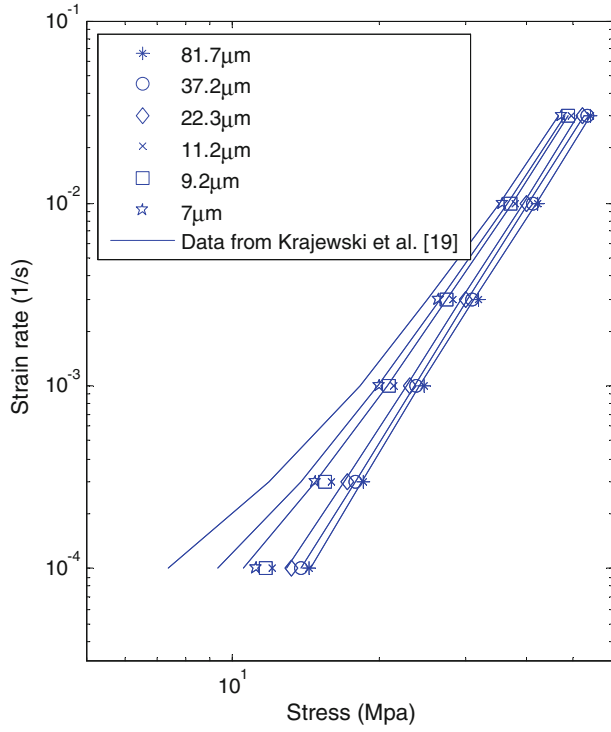
Fig. 9—Comparison of current simulation predictions without GBD with Krajewski *et al.*'s[19] data.

To investigate effect of each mechanism, the contribution of each deformation on total strain rate is defined as follows:

$$f_{CR} = \frac{\int_0^t \sqrt{D_{ij}^{CR} D_{ij}^{CR}} dt}{\int_0^t \sqrt{D_{ij}^{T} D_{ij}^{T}} dt}, \quad f_{GBS} = \frac{\int_0^t \sqrt{D_{ij}^{GBS} D_{ij}^{GBS}} dt}{\int_0^t \sqrt{D_{ij}^{T} D_{ij}^{T}} dt},$$

$$f_{GBD} = \frac{\int_0^t \sqrt{D_{ij}^{GBD} D_{ij}^{GBD}} dt}{\int_0^t \sqrt{D_{ij}^{T} D_{ij}^{T}} dt} \qquad [39]$$

where D_{ij}^{T} is the total deformation rate, f_{CR} is the fraction of crystal or intergranular deformation, f_{GBS} is the fraction from GBS, and f_{GBD} is the fraction from GBD.

Figures 10 through 12 show contributions of each mechanism for various grain sizes and strain rates.

In all Figures 10 through 12, a pronounced difference is observed between two distinct zones that were previously defined. Figure 10 shows that GBD is nearly zero for zone A, but it has a significant contribution in zone B. Therefore, it can be concluded that the difference between these two zones is basically from GBD. Knowing that material shows superplastic behavior in zone B, it is realized that GBD has significant role in superplastic forming. Hence, superplastic limits can be extended by promoting this mechanism.

Figure 12 shows the contribution of GBS. In this figure, a remarkable difference is observed between zones A and B. In zone A, the contribution of GBS decreases when the strain rate increases, but in zone B the behavior is the opposite. This remarkable change in these behaviors is because GBD is more pronounced in zone B but is less effective in zone A.
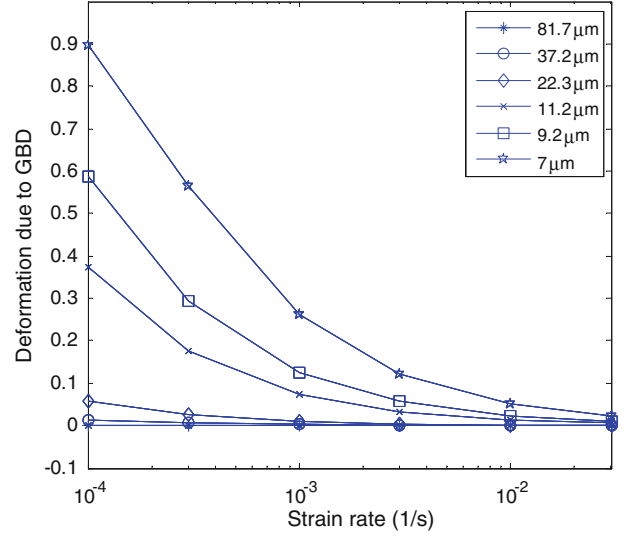

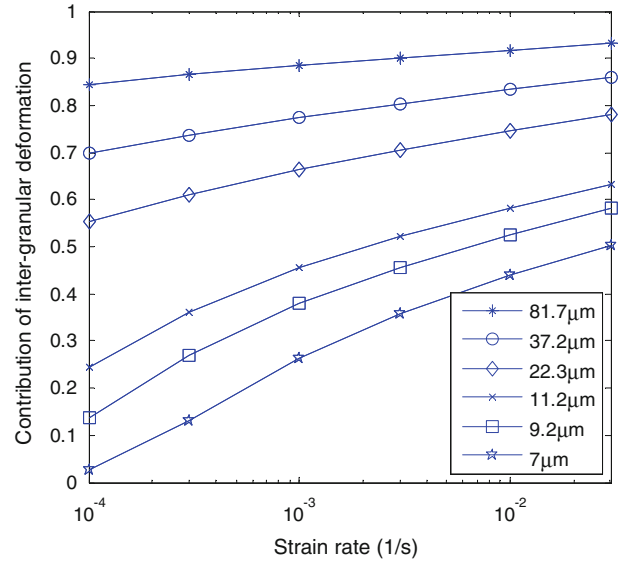Fig. 10—Contribution of GBD mechanism in total deformation.

Fig. 11—Contribution of intergranular deformation in total deformation.

In zone A where the dominant mechanisms are GBS and intergranular, flow stress changes slightly with grain size but in zone B where GBD is also effective, grain size has more effect on the flow stress. These results validate Eqs. [17] and [35], which express the effect of grain size on flow stress for GBS and GBD mechanisms.

B. Simulation of Multiaxial Stress States

After showing the validity of the model in uniaxial stress state, the model is examined for multidirectional stress states.

1. Yield loci from the model

Comparing the yield locus from the model with a well-known yield locus such as von Mises criterion can verify
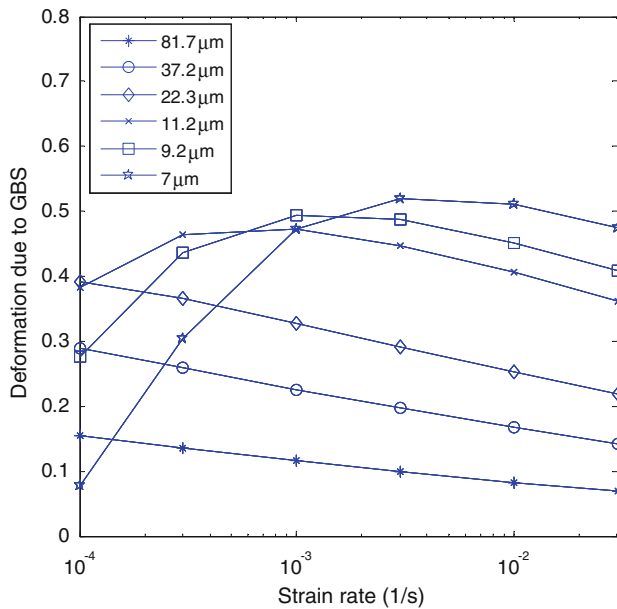
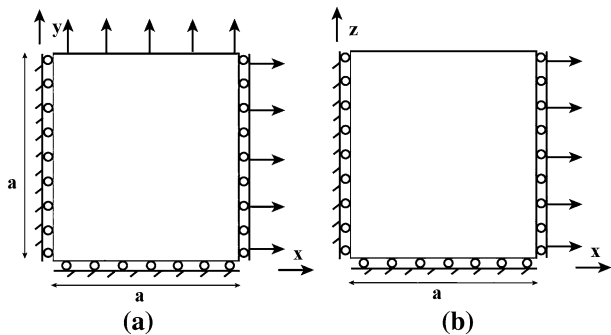Fig. 12—Contribution of GBS mechanism in total deformation.

Fig. 13—Boundary conditions for investigating yield loci (a) in xy plane (b) in xz plane.

the model in multidirectional stress states. To obtain the yield locus from the presented model, the material is subjected to two directional tension and compression tests with different ratios. As shown in Figure 13, symmetric conditions are applied on planes $x = 0$, $y = 0$, and $z = 0$; there is no traction on plane $z = a$; and the solid is subjected to a constant strain rate by displacing the plane $x = a$ and $y = a$. Also, the ratio of velocities in plane $x = a$ and $y = a$ differs from one simulation to another, but in all ratios, the velocities are chosen such that the effective strain rate remains constant

$$\sqrt{\dot{\varepsilon}_{ij}\dot{\varepsilon}_{ij}} = cte \qquad [40]$$

In Equation [40], the incompressibility rule is used to calculate strain rate in the z direction.

$$\dot{\varepsilon}_1 + \dot{\varepsilon}_2 + \dot{\varepsilon}_3 = 0 \qquad [41]$$

The simulations are performed for grain size = 7 μm and strain rate = 0.00011/s. where intergranular deformation, GBD, and GBS mechanisms are effective.

Figure 14 compares von Mises yield surface with yield loci obtained from the model assuming Taylor type polycrystalline, Taylor type polycrystalline with GBS, and Taylor type polycrystalline with both GBS and GBD mechanisms, respectively. These yield loci are obtained by using the material parameters reported in Table II. To compare the shape of the yield loci obtained from the model with the Mises yield locus, the same yield stress in pure tension for both models are assumed. As it can be shown from Figure 14, the yield loci shapes are very similar to von Mises criterion especially when GBD mechanism is taken into account.

Considering Eq. [35] and its similarity to von Mises criterion, this similarity in yield loci was expected. Yield loci show that boundary mechanisms are isotropic.

Researchers who experimentally studied yield locus for superplastic forming of Sn-38Pb at room temperature and Zn-22Al alloy at high temperature[2,45] also concluded that these materials are isotropic and their yield loci obey the von Mises yield criterion. Therefore, it can be concluded that the model can be used to predict material behavior in multidirectional stress states.

2. *Gas Pressure Forming Simulation*

The material model was implemented in FEM simulations of gas-pressure bulge-forming to show the ability of the model in situations where both multidirectional stress states and various strain rates exist. Five various grain sizes are modeled to show the ability of the model to predict material behavior considering all effective parameters. These cases were experimentally studied by Krajewski et al.[19] Table III shows initial sheet thickness of each case and its corresponding experimental gas pressure.

The experiments were performed at 723 K (450 °C). The formation was terminated prior to failure after 1800 seconds in each test. The dome height was measured after forming, and the relationship between the dome height and grain size was obtained. According to these experiments, increasing the grain size significantly decreases the dome height as is expected. Details of experimental procedure are reported in References 19 and 46.

ABAQUS Standard is used to simulate gas-pressure bulge-forming. The material model is applied through a user subroutine. The process is considered to be axisymmetric. A mesh sensitivity study is conducted to assure that element size is sufficiently fine to provide acceptable predictions of bulge displacements. For this purpose, simulations with one and two elements along the sheet thickness were carried out, and no significant change was observed in the dome height and stress field. Therefore, for all simulations (simulation for various grain sizes) two elements along the thickness are used. For this purpose, approximately 200 quadrilateral CAX4 elements with four integration points for various sheet thicknesses are used. Figure 15 shows initial mesh of one of the blanks. Figure 16 shows the deformed sheet.

The implicit formulation in ABAQUS requires the calculation of an initial elastic response; hence, a linear
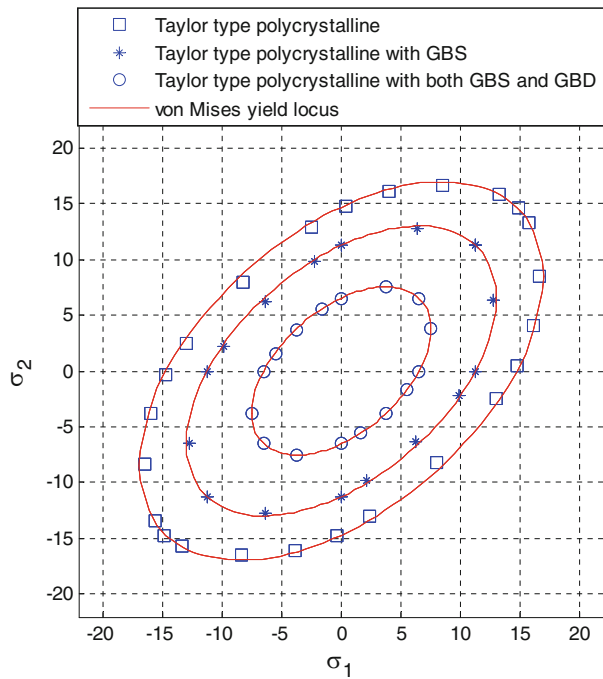
Fig. 14—Resulting yield loci from the Taylor type polycrystalline, the Taylor type polycrystalline with GBS, and the Taylor type polycrystalline with both GBS and GBD.

Table III. Initial Sheet Thickness and Pressure Related to Each Grain Size

Grain size (μm)	7.0	11.2	22.3	37.2	81.7
Gas pressure (MPa)	0.39	0.25	0.31	0.33	0.35
Sheet thickness (mm)	1.60	1.04	1.27	1.38	1.44

Fig. 15—Initial mesh of a blank used in gas-pressure bulge-forming simulation.

ramp type pressure is applied within 1 second and is then kept constant as was used in the experiments (1800 seconds). Plastic deformation was subsequently calculated for the duration of the simulation. The simulation results of dome heights *vs* grain sizes as well as experimental data are shown in Figure 17.

The predicted trends in dome height follow the trend in the experimental curve that shows a rapid decrease in dome height (for the finer grain sizes) as grain size increases and a slower decrease to a nearly constant value (for the coarser grain size materials). The disparity between theory and experiment for the finest grain size material is likely from the neglecting effects of hydrostatic pressure as has been mentioned by Eric *et al.*[46] They suggested that hydrostatic stress increases boundary deformations but does not affect the intergranular deformation. It is worth mentioning that the presented
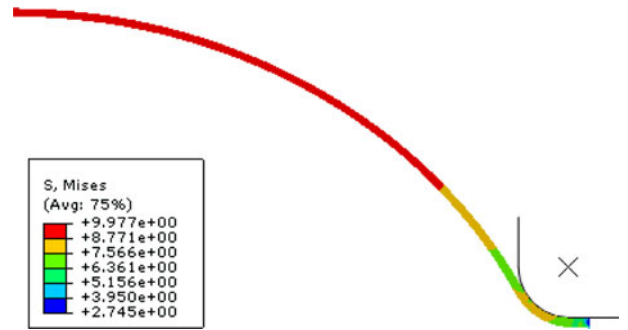

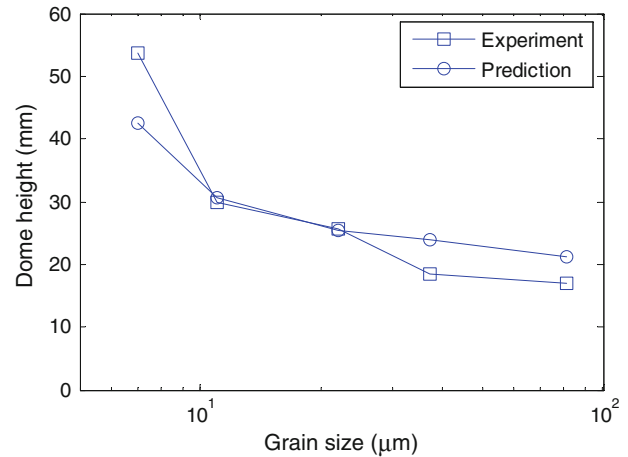Fig. 16—Final deformed sheet after 1800 s and applying a constant pressure.

Fig. 17—Simulation results for dome heights *vs* grain sizes compared with Krajewski *et al.*'s experimental data.[19]

model in this article can capture this effect by incorporating effect of normal stress on GBS by modifying Eq. 16. This will be implemented in our future works since it needs experimental calibrations.

3. *Tray forming simulation*

In this section, the proposed constitutive model is examined in a practical example. At first, the model is calibrated by tensile test values of AA5083 at 748 K (475 °C) with different strain rates by Luo *et al.*[47] Then, it is used to simulate superplastic gas pressure tray forming at the same temperature. In this process, a sheet is clamped on a die with a rectangular cavity of 200 mm width, 200 mm length, and 150 mm depth. Figure 18 shows one quarter of the die surface and the sheet. A die entrance radius of 20 mm makes the transition from the flange to the rectangular cavity. More details about tensile tests results and tray forming process have been reported by Luo *et al.*[47] In this process, the pressure is applied on the sheet for 1248 seconds; after this time, the sheet forms entirely on the die. After forming, the thickness of the part was measured along the line (AB) that connects the center of the part to midpoint of one edge.

ABAQUS EXPLICIT finite-element code is used to simulate this process. In the current simulation, the
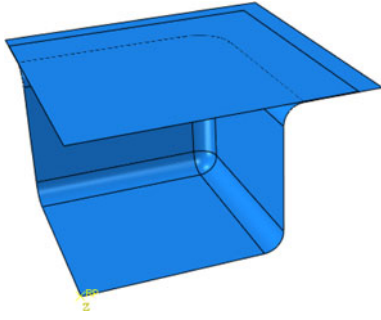
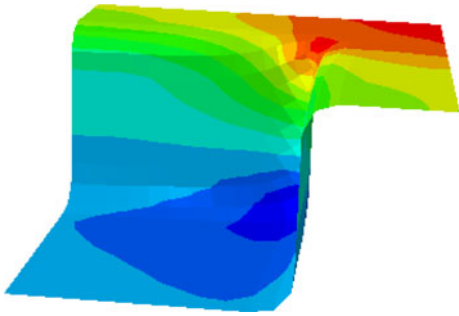Fig. 18—One quarter of the die surface and the sheet.

Fig. 19—Final shape of one quarter of the part.

Fig. 20—Predicted and measured sheet thicknesses along its width.

pressure history that is used in the real process[47] is applied on the sheet by a user amplitude routine (VUAMP). The sheet is meshed with 529 quadrilateral M3D4 elements and the die has 668 R3D4 elements. Figure 19 shows the final shape that is predicted by the current simulation. Figure 20 shows the predicted sheet thicknesses after 1248 seconds, *i.e.,* the same time that the measurements were performed. In this figure, the measured thicknesses are also added for comparison. It can be observed from this figure that the predicted thicknesses are in good agreement with measured values. The results obtained in this section prove that the model can be used for the simulation of industrial parts.

C. *Investigation of Model Sensitivity*

In this section, the effects of various constitutive parameters of the presented model in the results are investigated. This investigation will reveal the importance of each parameter in various circumstances. It is also helpful to investigate more about the effect of each mechanism in various circumstances. In this section, all parameters values are the same as those in Table II unless specified otherwise in the figure. In all figures, the effect of parameters are plotted for two small and large grain sizes to show their effects in the whole region that is considered in this article.

The effect of characteristic strain rate $\dot{\gamma}_0$ is shown in Figure 21. As it is observed from this figure, this parameter has a significant effect on the predicted stress for almost the entire region. This is in general agreement with experimental observation reported in Reference 15. Only for a grain size of 11.2 μm and strain rate less than
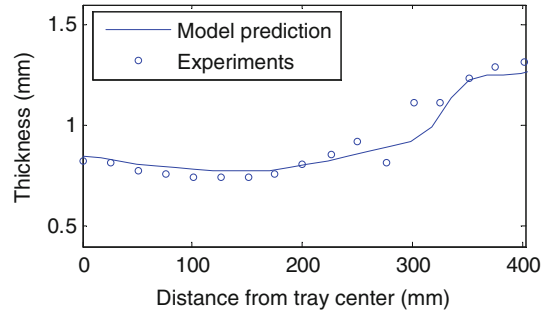
0.0011/s, this effect decreases. With regard to Figure 6, it can be concluded that effect of this parameter in region B is less than region A. Figure 11, which shows intergranular contribution in total deformation, also suggests a similar conclusion.

Figures 22 and 23 show the effects of GBS parameters including GBS preexponential η and threshold stress on the predicted stress, respectively. GBS parameters have a significant effect for grain size of 11.2 μm, but this effect sharply reduce for a grain size of 81.7 μm.

The effect of GBD coefficient K is illustrated in Figure 24. Comparing this figure with Figure 6 reveals that this parameter is only effective in zone B. This result confirms previous claim that GBD can be ignored for grain sizes more than 22.3 μm.

In general, it can be concluded that all the model parameters are effective, but some of them have a lesser effect in a certain zone. This change can also be explained by the role of each mechanism in various regions.

V. CONCLUSIONS

A new constitutive model for simulations of hot plastic forming has been proposed. The model considers grain boundary sliding, diffusion, and deformation within the grains. The accuracy and capability of the model were illustrated by comparing the predictions of the model with experimental data. New stress–strain-rate relationships were derived and presented for grain boundary sliding and grain boundary diffusion and the following results were obtained:

1. In deformations caused by the GBS mechanism, the strain rate has an inverse relation with the grain size so by increasing the grain size, the GBS deformation decreases.
2. In deformations caused by the GBD mechanism, the strain rate has an inverse relation with power three of grain size, so by increasing the grain size, the GBD deformation decreases more rapidly compared with GBS.
3. The stress–strain rate for grain boundary diffusion mechanism behaves similar to the Prandtl-Reuss flow rule.

The preceding predictions are in good agreement with the experimental expectations and observations
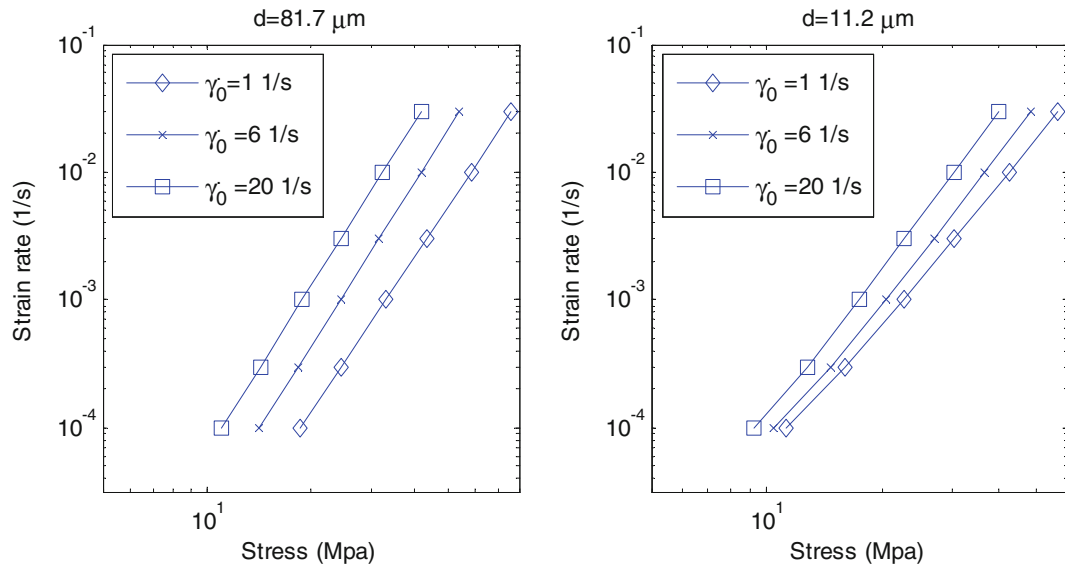
Fig. 21—Effect of characteristic strain rate $\dot{\gamma}_0$ on stress for grain sizes of 11.2 μm and 81.7 μm.
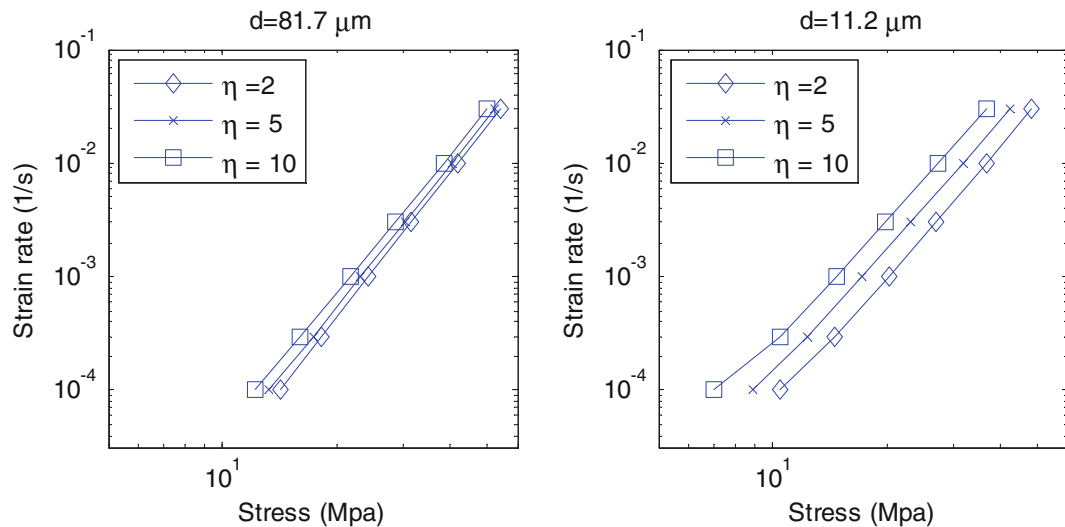

Fig. 22—Effect of grain boundary sliding preexponential on stress for grain sizes of 11.2 μm and 81.7 μm.

considered in this article. After using model in various simulations, the following results were obtained:

1. After calibration with only a few experiments, the presented model predicts the flow stresses close to the experimental data. The model can be used to predict the flow stresses for a vast range of grain sizes and strain rates.
2. The model can be used for AA5083 at 723 K (450 °C) with grain sizes more than 22.3 μm without considering the GBD effect.
3. Transition from zone A to B that exists in experimental observations is caused by GBD deformation.
4. GBD has a significant role in superplastic forming.
5. The resulting yield locus from the model predicted the von Mises criterion without any preassumptions.

6. The model could predict deformations of bulge forming tests and tray forming process. It is expected that it can also predict deformation of other multiaxial processes.
7. A sensitivity analysis of affecting constitutive parameters in the model showed the following:

   • GBS parameters have a significant effect for small grain sizes, but this effect drastically reduces for larger grain sizes.
   • GBD coefficient is only effective for small grain sizes and low strain rates.
   • Characteristic strain rate $\dot{\gamma}_0$ in each slip system has a significant effect on predicted stress almost for the entire region.
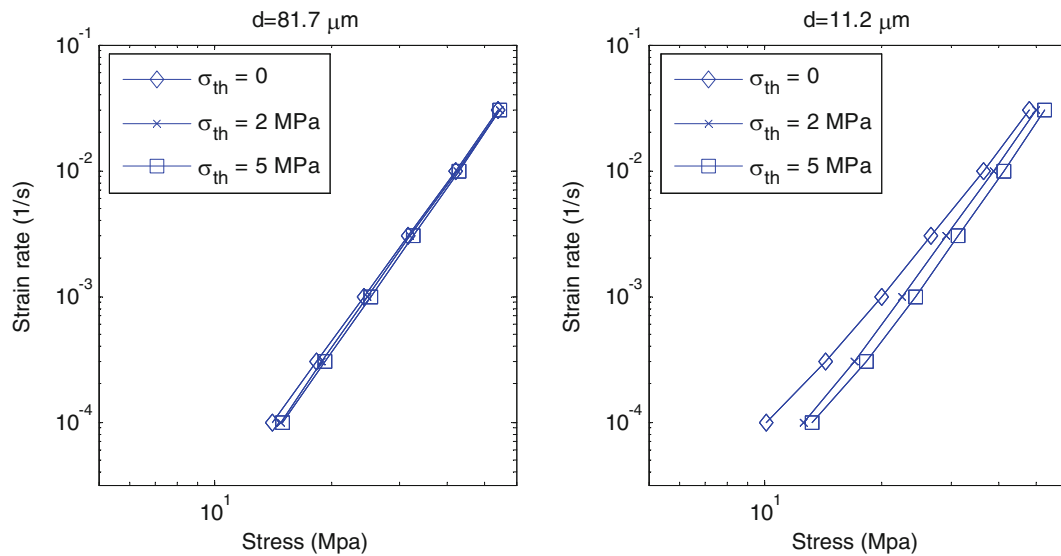
Fig. 23—Effect of threshold stress σ_{th} on stress for grain sizes of 11.2 μm and 81.7 μm.
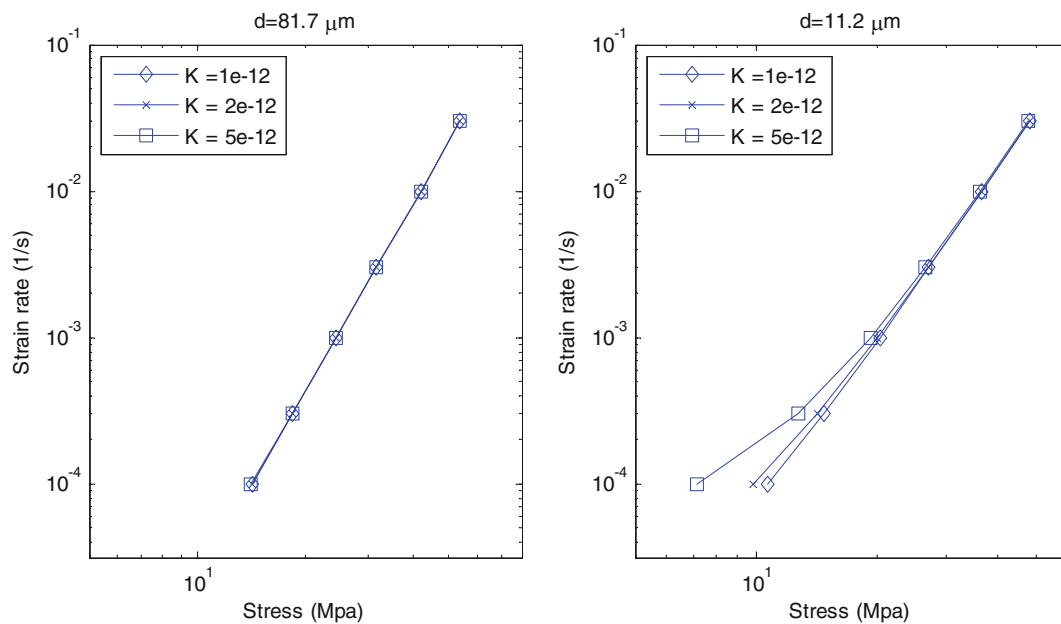

Fig. 24—Effect of grain boundary diffusion coefficient K on stress for grain sizes of 11.2 μm and 81.7 μm.

The model requires heavy computations at each material point. Therefore, its application in finite-element simulations that have several integration points is time consuming.

The computations did not consider grain growth and its consequent hardening effects. Also, the effect of hydrostatic pressure on the deformation of fine grain materials can be investigated by considering the effect of normal stress on GBS. These will be covered in author's future work.

REFERENCES

1. A.J. Barnes: *J. Mater. Eng. Perform.*, 2007, vol. 16, pp. 440–54.
2. H.L. Xing, C.W. Wang, K.F. Zhang, and Z.R. Wang: *J. Mater. Process. Tech.*, 2004, vol. 151, pp. 196–202.
3. J. Bonet, A. Gil, R.D. Wood, R. Said, and R.V. Curtis: *Comput. Meth. Appl. Mech. Eng.*, 2006, vol. 195, pp. 6580–6603.
4. M.T. Eric, L. Hector, R. Verma, P. Krajewski, and J.-K. Chang: *J. Mater. Eng. Perform.*, 2010, vol. 19, pp. 488–94.
5. O.D. Sherby and J. Wadsworth: *Progr. Mater. Sci.*, 1989, vol. 33, pp. 169–221.
6. M.A. Khaleel, K.I. Johnson, C.H. Hamilton, and M.T. Smith: *Int. J. Plast.*, 1998, vol. 14, pp. 1133–54.
7. M.K. Khraisheh, F.K. Abu-Farha, M.A. Nazzal, and K.J. Weinmann: *CIRP Annals—Manufact. Technol*, 2006, vol. 55, pp. 233–36.
8. S.G. Luckey, Jr., P.A. Friedman, and K.J. Weinmann: *J. Mater. Process. Tech.*, 2007, vol. 194, pp. 30–37.

9. M.A. Nazzal, M.K. Khraisheh, and F.K. Abu-Farha: *J. Mater. Process. Tech.*, 2007, vol. 191, pp. 189–92.
10. H. Raman, G. Luckey, G. Kridli, and P. Friedman: *J. Mater. Eng. Perform.*, 2007, vol. 16, pp. 284–92.
11. R. Verma, L. Hector, P. Krajewski, and E. Taleff: *JOM*, 2009, vol. 61, pp. 29–37.
12. G.Y. Li, M.J. Tan, and K.M. Liew: *J. Mater. Process. Tech.*, 2004, vol. 150, pp. 76–83.
13. G. Giuliano: *Mater. Des.*, 2008, vol. 29, pp. 1330–33.
14. N. Chandra: *Int. J. Non-Lin. Mech.*, 2002, vol. 37, pp. 461–84.
15. S. Agarwal, C. Briant, P. Krajewski, A. Bower, and E. Taleff: *J. Mater. Eng. Perform.*, 2007, vol. 16, pp. 170–78.
16. A.F. Bower and E. Wininger: *J. Mech. Phys. Solids*, 2004, vol. 52, pp. 1289–1317.
17. D.E. Cipoletti, A.F. Bower, Y. Qi, and P.E. Krajewski: *Mater. Sci. Eng. A*, 2009, vol. 504, pp. 175–82.
18. N. Du, A.F. Bower, P.E. Krajewski, and E.M. Taleff: *Mater. Sci. Eng. A*, 2008, vol. 494, pp. 86–91.
19. P.E. Krajewski, L.G. Hector, Jr., N. Du, and A.F. Bower: *Acta Mater*, 2010, vol. 58, pp. 1074–86.
20. J.H. Kim, S.L. Semiatin, and C.S. Lee: *Acta Mater.*, 2003, vol. 51, pp. 5613–26.
21. T.G. Langdon: *Acta Metall. Mater.*, 1994, vol. 42, pp. 2437 43.
22. F.C. Liu and Z.Y. Ma: *Scripta Mater.*, 2010, vol. 62, pp. 125–28.
23. S.S. Park, H. Garmestani, G.T. Bae, N.J. Kim, P.E. Krajewski, S. Kim, and E.W. Lee: *Mater. Sci. Eng. A*, 2006, vols. 435–436, pp. 687–92.
24. M.-A. Kulas, W.P. Green, E.M. Taleff, P.E. Krajewski, and T.R. Mcnelley: *Metall. Mater. Trans. A*, 2005, vol. 36A, pp. 1249–61.
25. W. Green, M.-A. Kulas, A. Niazi, E. Taleff, K. Oishi, P. Krajewski, and T. McNelley: *Metall. Mater. Trans. A*, 2006, vol. 37A, pp. 2727–38.
26. T.R. McNelley, K. Oh-Ishi, A.P. Zhilyaev, S. Swaminathan, P.E. Krajewski, and E.M. Taleff: *Metall. Mater. Trans. A*, 2008, vol. 39A, pp. 50–64.
27. K. Inal, K.W. Neale, and A. Aboutajeddine: *Int. J. Plast.*, 2005, vol. 21, pp. 1255–66.
28. K. Inal, P.D. Wu, and K.W. Neale: *Int. J. Plast.*, 2000, vol. 16, pp. 635–48.
29. K. Inal, P.D. Wu, and K.W. Neale: *Int. J. Solid. Struct.*, 2002, vol. 39, pp. 3469–86.
30. K. Inal, P.D. Wu, and K.W. Neale: *Int. J. Solid. Struct.*, 2002, vol. 39, pp. 983–1002.
31. K. Inal, P.D. Wu, and K.W. Neale: *Modell. Simul. Mater. Sci. Eng.*, 2002, vol. 10, pp. 237–52.
32. P. Tugcu, K.W. Neale, P.D. Wu, and K. Inal: *Int. J. Plast.*, 2004, vol. 20, pp. 1603–53.
33. A.C.F. Cocks: *Mech. Mater.*, 1992, vol. 13, pp. 165–74.
34. J. Pan and A.C.F. Cocks: *Comput. Mater. Sci.*, 1993, vol. 1, pp. 95–109.
35. F. Dunne and N. Petrinic: *Introduction to Computational Plasticity*, Oxford University Press Inc, Oxford, U.K., 2006.
36. D. Peirce, R.J. Asaro, and A. Needleman: *Acta Metall.*, 1982, vol. 30, pp. 1087–1119.
37. D. Peirce, R.J. Asaro, and A. Needleman: *Acta Metall.*, 1983, vol. 31, pp. 1951–76.
38. R.J. Asaro: *J. Appl. Mech.*, 1983, vol. 50, pp. 921–34.
39. R.J. Asaro, W.H. John, and Y.W. Theodore: *Advances in Applied Mechanics*, vol. 23, Elsevier, Atlanta, GA, 1983, pp. 1–115.
40. Y. Huang: *A User Material Subroutine Incorporating Single Crystal Plasticity in the ABAQUS Finite Element Program*, Harvard University, Cambridge, MA, 1992.
41. T. Iwakuma and S. Nemat-Nasser: *Proc. Royal Soc. London*, 1984, vol. 394, no. 1806, pp. 87–119.
42. A. Molinari, G.R. Canova, and S. Ahzi: *Acta Metall.*, 1987, vol. 35, pp. 2983–94.
43. G.Z. Sachs and D. Verein: *Der Verein dutsher Ingenieur*, 1928, vol. 72, p. 734.
44. G.I. Taylor: *JIM*, 1938, vol. 62, pp. 307–24.
45. Z.R. Wang, Y.W. Xu, and D.J. Guo: *Proceedings of the First National Meeting on Plastic Mechanics in Chinese*, 1986.
46. M.T. Eric, G.H. Louis, R.B. John, V. Ravi, and E.K. Paul: *Acta Mater.*, 2009, vol. 57, pp. 2812–22.
47. Y. Luo, S.G. Luckey, P.A. Friedman, and Y. Peng: *Int. J. Mach Tools Manufact.*, 2008, vol. 48, pp. 1509–18.